

# SCIENTIFIC REPORTS



OPEN

## A sandwich-type electrochemical immunosensor based on the biotin- streptavidin-biotin structure for detection of human immunoglobulin G

Received: 10 December 2015

Accepted: 17 February 2016

Published: 07 March 2016

Yueyun Li<sup>1,2</sup>, Yihe Zhang<sup>1</sup>, Liping Jiang<sup>2</sup>, Paul K. Chu<sup>3</sup>, Yunhui Dong<sup>2</sup> & Qin Wei<sup>4</sup>

A sandwich-type immunosensor is designed and fabricated to detect the human immunoglobulin G (HIgG) using polyaniline and tin dioxide functionalized graphene (GS-SnO<sub>2</sub>-PAN) as the platform and biotin-functionalized amination magnetic nanoparticles composite (B-Fe<sub>3</sub>O<sub>4</sub>@APTES) as the label. GS-SnO<sub>2</sub>-PAN is used as the sensing agent to capture the primary anti-HIgG (Ab<sub>1</sub>) and SnO<sub>2</sub> reduces the stack of GS. The B-Fe<sub>3</sub>O<sub>4</sub>@APTES with a large surface area and excellent biocompatibility captures second antibody (Ab<sub>2</sub>) efficiently based on the highly selective recognition of streptavidin to biotinylated antibody. The B-Fe<sub>3</sub>O<sub>4</sub>@APTES has better electro-catalytic activity in the reduction of hydrogen peroxide (H<sub>2</sub>O<sub>2</sub>) and the "biotin-streptavidin-biotin" (B-SA-B) strategy leads to signal amplification. Under optimal conditions, the immunosensor has a wide sensitivity range from 1 pg/L to 10 ng/L and low detection limit of 0.33 pg/L (S/N = 3) for HIgG. The immunosensor has high sensitivity, fast assay rate, as well as good reproducibility, specificity, and stability especially in the quantitative detection of biomolecules in serum samples.

Immunoglobulin (Ig) is an important component in the immune system and plays an important role in recognizing bacteria and viruses. There are five types of Igs in the human plasma and human immunoglobulin G (HIgG) is the most important one accounting for about 75% of the total Igs<sup>1,2</sup>. HIgG is effective in the treatment of humoral mediated neurological autoimmune diseases and has been reported to improve the outcome in some neuromyelitis optica patients<sup>3</sup>.

Electrochemical immunosensors based on the antigen-antibody specific reactions have recently attracted much interest and many immunosensors have been used for the detection of HIgG<sup>4,5</sup>. Compared to conventional immunoassays such as enzyme linked immunosorbent assays (ELISA)<sup>6</sup>, fluoroimmunoassays<sup>7</sup>, and chemiluminescence immunoassays<sup>8</sup>, electrochemical immunosensors are excellent in the detection of disease-related proteins due to inherent advantages including simple pretreatment procedures, short analytical time, precise current measurements, and inexpensive instrumentation<sup>9–12</sup>. In order to improve the sensitivity and selectivity of electrochemical immunosensors, interface materials serving as good carriers or bridges for efficient immobilization of proteins are critical<sup>13</sup>. The physical and chemical properties of the interface play a crucial role in the assay performance<sup>13,14</sup>.

SnO<sub>2</sub> nanoparticles are used widely in biosensors on account of the high electron mobility as well as good chemical and thermal stability<sup>15</sup> and graphene sheets (GS) have excellent conductivity and large specific surface area. Yao *et al.* developed an *in situ* synthesis method to produce tin dioxide - graphene (GS-SnO<sub>2</sub>) nanocomposite

<sup>1</sup>Beijing Key Laboratory of Materials Utilization of Nonmetallic Minerals and Solid Wastes, National Laboratory of Mineral Materials, School of Materials Science and Technology, China University of Geosciences, Beijing, 100083, P. R. China. <sup>2</sup>School of Chemical Engineering, Shandong University of Technology, Zibo, 255049, P. R. China.

<sup>3</sup>Department of Physics & Materials Science, City University of Hong Kong, Tat Chee Avenue, Kowloon, Hong Kong, China. <sup>4</sup>Key Laboratory of Chemical Sensing & Analysis in Universities of Shandong, School of Chemistry and Chemical Engineering, University of Jinan, Jinan, 250022, P.R. China. Correspondence and requests for materials should be addressed to Y.Z. (email: zyh@cugb.edu.cn) or Q.W. (email: sdjndxwq@163.com)

as the anode in lithium-ion batteries<sup>16</sup> and Lu *et al.* investigated the electrochemical behavior of GS-SnO<sub>2</sub> composite films in supercapacitors<sup>17</sup>. However, there have been few reports on the use of GS-SnO<sub>2</sub> nanocomposite in electrochemical sensors. SnO<sub>2</sub> nanoparticles could be distributed on GS followed by the *in situ* synthesis of polyaniline (PAN) on the GS-SnO<sub>2</sub> composite to obtain polyaniline functionalization of tin dioxide/graphene (GS-SnO<sub>2</sub>-PAN). PAN improves electron transfer due to the good electrical conductivity. SnO<sub>2</sub> and PAN adhere on the GS to reduce the GS stack and form a sandwich-like structure composite. The GS-SnO<sub>2</sub>-PAN can be used as the sensing agent for immobilization of primary antibody (Ab<sub>1</sub>) to improve the electrochemical performance of the modified electrode.

An amplification strategy has been proposed to improve the sensitivity of electrochemical immunosensors using the biotin labeled protein-streptavidin (SA) network complex. SA, a 66 kDa protein has been widely used in immunohistochemistry<sup>18</sup> and immunoassay<sup>19</sup> due to its high specificity and strong affinity for biotin<sup>20</sup>. In the immunoassay, the high affinity of SA and biotin<sup>21</sup> benefits the capture of specific classes of proteins<sup>22</sup>.

In this work, an electrochemical immunosensor is described for quantitative detection of HIgG by using the biotin-functionalized amination magnetic nanoparticles composite (B-Fe<sub>3</sub>O<sub>4</sub>@APTES) and GS-SnO<sub>2</sub>-PAN for signal amplification. The B-Fe<sub>3</sub>O<sub>4</sub>@APTES is used as a label for Ab<sub>2</sub> through catalyzing the electrochemical reaction of hydrogen peroxide (H<sub>2</sub>O<sub>2</sub>). The 3-aminopropyltriethoxysilane (APTES) functionalized Fe<sub>3</sub>O<sub>4</sub> (Fe<sub>3</sub>O<sub>4</sub>@APTES) can bind biotin through the exposed active amino groups and carboxy group on biotin<sup>23</sup>. This "biotin-streptavidin-biotin" (B-SA-B) structure is utilized to combine Ab<sub>2</sub> and the marker (B-Fe<sub>3</sub>O<sub>4</sub>@APTES). The cross-shaped SA has one free biotin-binding site available for a biotinylated antibody (B-Ab<sub>2</sub>) and the other three binding sites are conjugated with a 3 equimolar ratio of B-Fe<sub>3</sub>O<sub>4</sub>@APTES to achieve triple-amplification. Additionally, the B-Fe<sub>3</sub>O<sub>4</sub>@APTES can be connected repeatedly by SA connection SA/B-Fe<sub>3</sub>O<sub>4</sub>@APTES for further multiple amplification signals. The novel immunosensor shows high sensitivity, fast assay speed, wide linear detection range, and low detection limit has potential applications in quantitative detection of HIgG.

## Results and Discussion

**Characterization of GS-SnO<sub>2</sub>-PAN composites.** The morphology of GS-SnO<sub>2</sub> and GS-SnO<sub>2</sub>-PAN is examined by SEM. As shown in Fig. 1A, irregular SnO<sub>2</sub> grains are distributed on the GS which resembles a piece of wrinkled paper. The SnO<sub>2</sub> nanoparticles with positive surface charges in a specific pH range can interact with GS by physical sorption, electrostatic binding, or charge transfer to produce a sandwich structure<sup>24</sup>. The EDS results reveal C, O, and Sn (Fig. 1B) and the presence of SnO<sub>2</sub> can prevent stacking of GS layers and improve the dispersion. As shown in Fig. 1C, GS-SnO<sub>2</sub>-PAN has a smooth surface and the white SnO<sub>2</sub> nanoparticles are covered by PAN. EDS conducted on GS-SnO<sub>2</sub>-PAN (Fig. 1D) confirms the presence of PAN showing an obvious N signal. The PAN increases the distance between layers of GS-SnO<sub>2</sub> and Ab<sub>1</sub> can better be immobilized on the GS-SnO<sub>2</sub>-PAN. The TEM image of GS-SnO<sub>2</sub> (Fig. 1E) and GS-SnO<sub>2</sub>-PAN (Fig. 1F) characterized the dispersion of the SnO<sub>2</sub>, GS and PAN. As shown in Fig. 1E,F, it can be seen that SnO<sub>2</sub> with diameters of approximately 4 nm evenly dispersed on the surface of GS. The lattice structure of PAN, GS, SnO<sub>2</sub> is evidently. The XRD patterns of the GS-SnO<sub>2</sub> nanocrystals and as-prepared GS-SnO<sub>2</sub>-PAN composites are shown in Fig. 2D. Figure 2D(a) shows the XRD pattern of the GS-SnO<sub>2</sub> composite. The major diffraction peaks from bare SnO<sub>2</sub> at 26.5°, 33.9°, 51.8°, and 65.8° can be indexed to (110), (101), (211), and (301) of the tetragonal SnO<sub>2</sub> nanocrystals<sup>25,26</sup>. The broad diffraction patterns indicate small particle size of SnO<sub>2</sub>. The GS shows the (100) diffraction peak<sup>27</sup> which coincides with the (110) diffraction peak of SnO<sub>2</sub>. There are no observable impurity peaks and no graphite peak at 26.6° is observed from GS-SnO<sub>2</sub>, suggesting that agglomeration of GS is inhibited by the SnO<sub>2</sub> nanoparticles on the surface and good dispersion in the composites. Figure 2D(b) shows the XRD pattern of the GS-SnO<sub>2</sub>-PAN composite. The peak positions are consistent but the intensity of GS-SnO<sub>2</sub>-PAN is lower than that of GS-SnO<sub>2</sub> T because of introduction of PAN to the surface. The GS-SnO<sub>2</sub>-PAN shows only one weak broad (002) peak in Fig. 2D(b) and it may be due to the corrugated pore structure of GS-SnO<sub>2</sub>-PAN<sup>28–30</sup>.

In order to evaluate the formation of GS-SnO<sub>2</sub>-PAN composites, FTIR is performed (Fig. 2E). With regard to PAN, the peaks at 1562 and 1485 cm<sup>-1</sup> correspond to the C=C stretching modes in quinoid and benzenoid ring whereas those at 1297, 1130 and 799 cm<sup>-1</sup> are attributed to C–N stretching, C=N stretching, and C–C stretching in the benzenoid ring, respectively<sup>31,32</sup>. As shown in Fig. 2E, the peaks from the GS-SnO<sub>2</sub>-PAN composite are characteristic ones for PAN and Sn–O stretching indicating successful synthesis of GS-SnO<sub>2</sub>-PAN.

**Characterization of Fe<sub>3</sub>O<sub>4</sub>@APTES composites.** The morphology of the Fe<sub>3</sub>O<sub>4</sub>@APTES (Fig. 2A) is examined by scanning electron microscopy (SEM). As shown in Fig. 3, the Fe<sub>3</sub>O<sub>4</sub>@APTES particles were an approximate spherical shape whose average diameter is 100 nm. XRD is performed on the Fe<sub>3</sub>O<sub>4</sub> and Fe<sub>3</sub>O<sub>4</sub>@APTES nanoparticles (Fig. 2B). The diffraction peaks are broadened due to the small crystallite size. The diffraction peaks in Fig. 2B (a) ( $2\theta = 30.2^\circ, 35.5^\circ, 43.1^\circ, 57.1^\circ$  and  $62.8^\circ$ ) correspond to (111), (220), (311), (400), (511), and (440) of Fe<sub>3</sub>O<sub>4</sub><sup>33,34</sup>. The average crystallite size is 100 nm. The same characteristic peaks can be found from Fig. 2B(b) illustrating that the characteristic peaks do not change but only the peak intensity and width after coating with amino-silane indicating that the crystalline structure of the modified nanoparticles is not varied. In addition, the coating process does not cause growth to and affect the physical properties of the magnetite particles<sup>35</sup>. No impurities are detected.

The FTIR spectra acquired from Fe<sub>3</sub>O<sub>4</sub> and Fe<sub>3</sub>O<sub>4</sub>@APTES are depicted in Fig. 2C. The peaks at 563 and 580 cm<sup>-1</sup> represent characteristic absorption of Fe–O confirming the presence of magnetite nanoparticles<sup>36,37</sup>, but the Fe–O–Si bond cannot be observed from Fig. 2C(a). It appears at around 578 cm<sup>-1</sup> and overlaps the Fe–O vibration of magnetite nanoparticles<sup>38,39</sup>. Adsorption of silane polymer onto the magnetite particles is confirmed by bands at 1111, 1047, and 1018 cm<sup>-1</sup> which correspond to the Si–O–H and Si–O–Si groups. The bands at 895 and 794 cm<sup>-1</sup> are due to stretching of Si–O–H and vibration of OH on the surface of magnetite. For the Fe<sub>3</sub>O<sub>4</sub>@APTES, Si–O–Si stretching is verified by the band at 1122 cm<sup>-1</sup><sup>39</sup>. The two broad band at

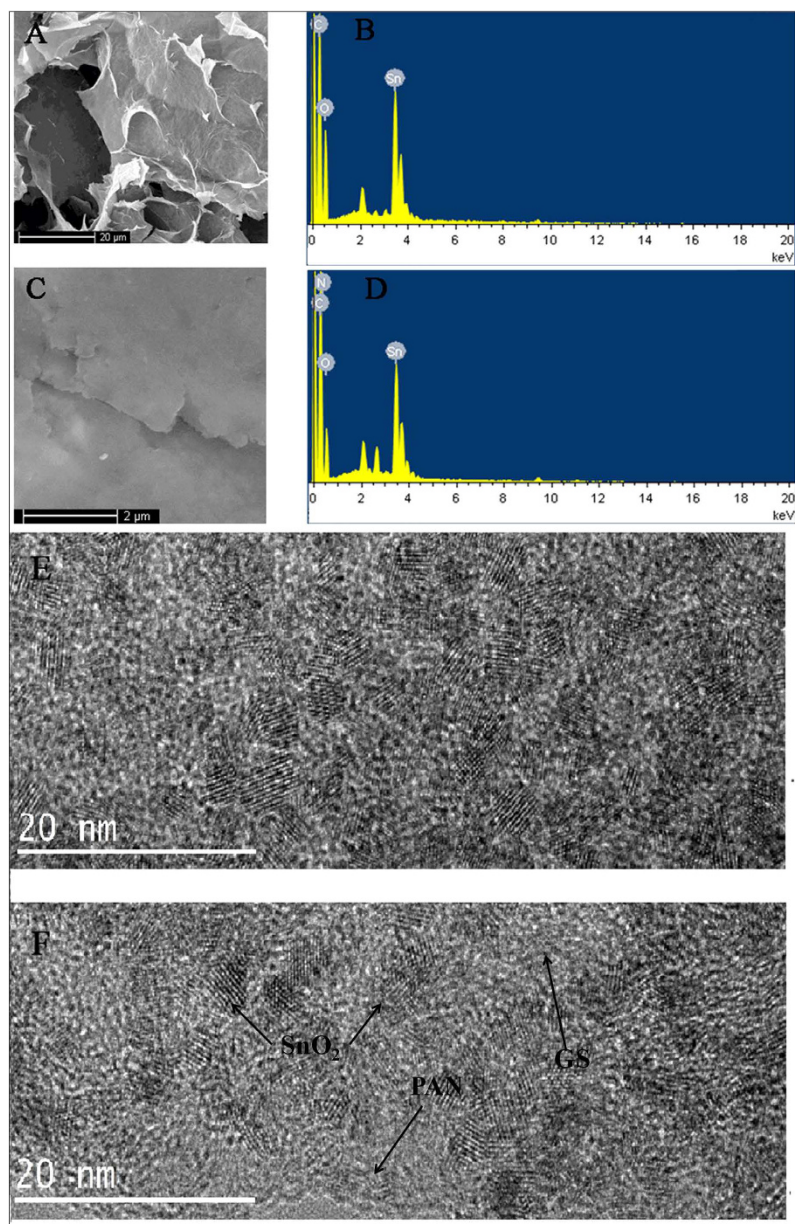


**Figure 1.** (A) SEM image of GS-SnO<sub>2</sub>; (B) EDS spectrum of GS-SnO<sub>2</sub>; (C) SEM image of GS-SnO<sub>2</sub>-PAN; (D) EDS spectrum of GS-SnO<sub>2</sub>-PAN; (E) HR-TEM image of GS-SnO<sub>2</sub>; (F) HR-TEM image of GS-SnO<sub>2</sub>-PAN.

3419 and 1653 cm<sup>-1</sup> can be ascribed to the N-H stretching vibration and NH<sub>2</sub> bending of the free NH<sub>2</sub> group, respectively<sup>40,41</sup>. As shown in Fig. 2C(b), the broad stretching peak at 3430 cm<sup>-1</sup> is the bending mode of free NH<sub>2</sub> groups in APTES<sup>42</sup>. The peak at 1431 cm<sup>-1</sup> is related to the methylene group and that at 1664 cm<sup>-1</sup> indicates C=O stretching in the carboxyl group<sup>43</sup>. The results show that the Fe<sub>3</sub>O<sub>4</sub> is functionalized with amino groups and consistent with previous reports<sup>44,45</sup>.

**Characterization of the immunosensor.** To characterize the sandwich-type immunosensor, CV is conducted in 5 mM K<sub>3</sub>[Fe(CN)<sub>6</sub>] solution (Fig. 3A). The GS-SnO<sub>2</sub>-PAN (curve b) is modified on a bare GCE (curve a) and the redox peak decreases because of lower electrical conductivity. Then Ab<sub>1</sub> (curve c), BSA (curve d), HlgG (curve e), and B-Ab<sub>2</sub> (curve f) are modified layer-by-layer on the electrode and the redox peak current declines gradually. The results suggest that the non-conductive bioactive substances reduce the efficiency of electron transfer. Finally, the SA (curve g) and B-Fe<sub>3</sub>O<sub>4</sub>@APTES (curve h) are modified on the electrode surface and the peak current decreases again demonstrating successful capture of SA and B-Fe<sub>3</sub>O<sub>4</sub>@APTES and that the immunocomplex inhibits electron transfer.

The A.C. impedance method is adopted to characterize the sandwich-type electrochemical immunosensor (Fig. 3B). The Nyquist plots are acquired from 1 to 10<sup>5</sup> Hz at 0.24 V in the solution containing 0.1 M KCl and 2.5 mM Fe(CN)<sub>6</sub><sup>3-</sup>/Fe(CN)<sub>6</sub><sup>4-</sup>. The high-frequency region of the impedance plot shows a semicircle related to

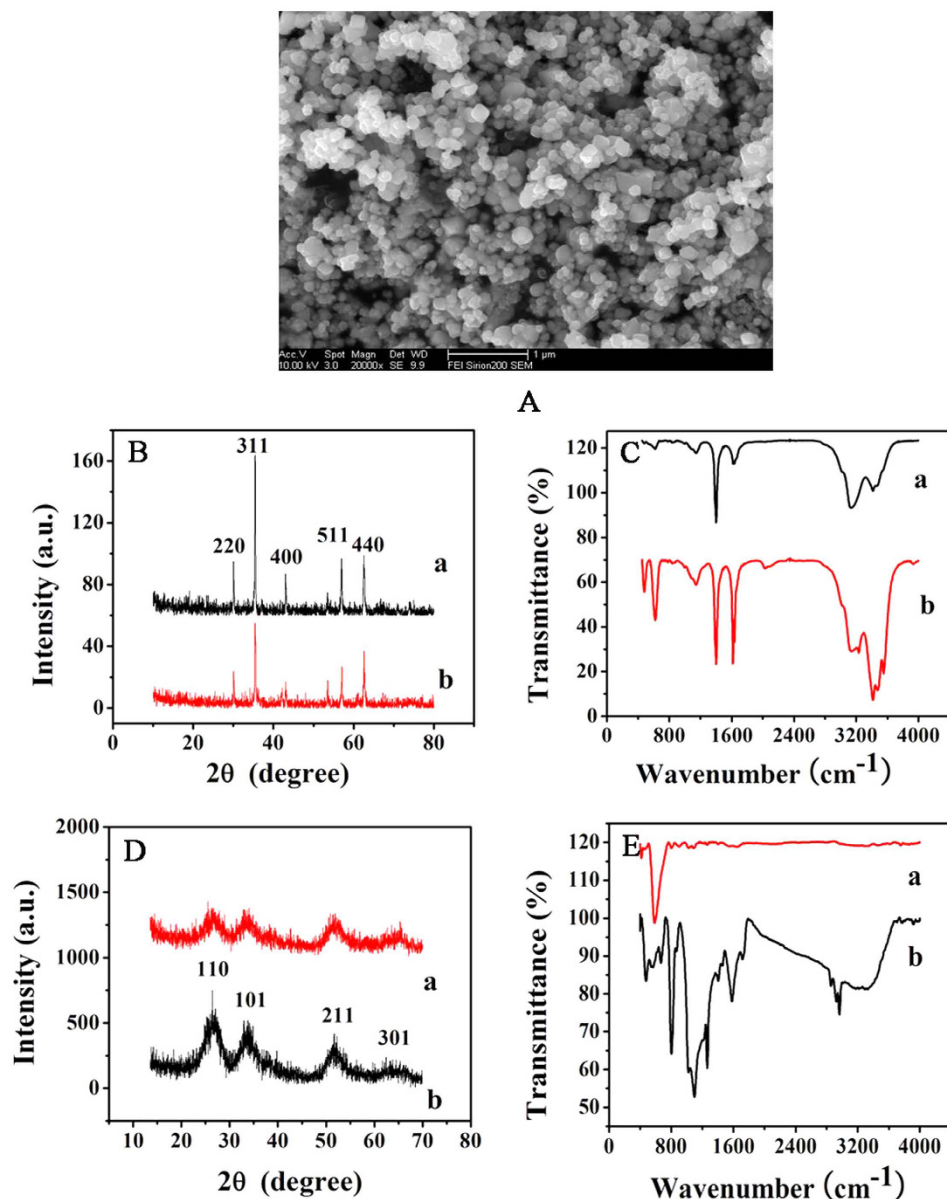


**Figure 2.** (A) SEM image of magnetite nanoparticles Fe<sub>3</sub>O<sub>4</sub>@APTES; (B) XRD spectra of (a) Fe<sub>3</sub>O<sub>4</sub> and (b) Fe<sub>3</sub>O<sub>4</sub>@APTES; (C) FTIR spectra of (a) Fe<sub>3</sub>O<sub>4</sub> and (b) Fe<sub>3</sub>O<sub>4</sub>@APTES; (D) XRD images of (a) GS-SnO<sub>2</sub>-PAN and (b) GS-SnO<sub>2</sub>; (E) FTIR spectra of (a) GS-SnO<sub>2</sub>-PAN and (b) GS-SnO<sub>2</sub>.

the redox probe Fe(CN)<sub>6</sub><sup>3-</sup>/Fe(CN)<sub>6</sub><sup>4-</sup> and the semicircle diameter is equal to the resistance. The Warburg line in the low-frequency region corresponds to the diffusion step of the overall process. The resistance can be estimated from the diameter of the semicircle part at higher frequencies in the Nyquist plot. The bare GCE (curve a) shows a small resistance. Gradual increase in the impedance of the electrode surface with addition of GS-SnO<sub>2</sub>-PAN (curve b), Ab<sub>1</sub> (curve c), BSA (curve d), HlgG (curve e), B-Ab<sub>2</sub> (curve f), SA (curve g), and B-Fe<sub>3</sub>O<sub>4</sub>@APTES (curve h) demonstrates that biologically active substances hinder electron transfer between the working electrode and electrolyte implying successful capture.

In order to demonstrate the multiple amplification effect of the B-SA-B system, the one-off modified immunosensor is further modified with SA and B-Fe<sub>3</sub>O<sub>4</sub>@APTES. The amperometric *i-t* curve (Fig. 3C) shows that the catalytic ability of the modified immunosensor (b) is 8 times than that of the one-off modified immunosensor (a).

**Optimization of experimental conditions.** To obtain optimal electrochemical signals, optimization of the experimental conditions including pH and Fe<sub>3</sub>O<sub>4</sub>@APTES concentration is necessary. The pH of the solution has a significant effect on the electrochemical behavior of the immunosensor because the activity of the antigen and antibody may be influenced by the highly acidic or alkaline surroundings<sup>46,47</sup>. In order to optimize the pH, a series of PBS with the pH from 5.0 to 8.0 is prepared. As shown in Fig. 4A, the current increases initially, reaches a maximum value at a pH of 6.0, and then decreases. Therefore, 6.0 is the optimal pH.

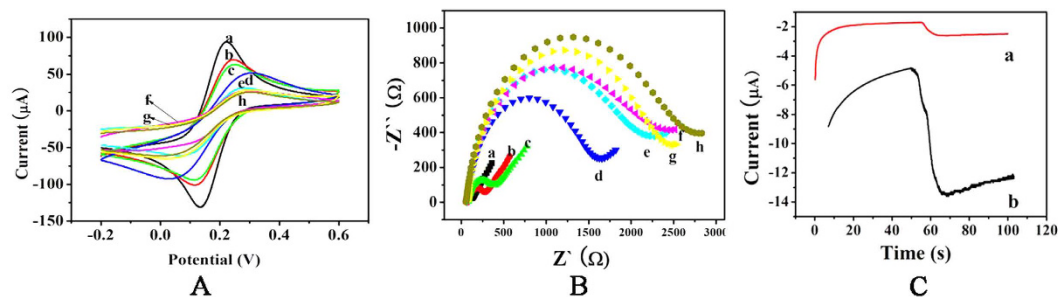


**Figure 3.** (A) CVs of the GCE (curve a), GS-SnO<sub>2</sub>-PAN/GCE (curve b), Ab<sub>1</sub>/GS-SnO<sub>2</sub>-PAN/GCE (curve c), BSA/Ab<sub>1</sub>/GS-SnO<sub>2</sub>-PAN/GCE (curve d), HIgG/BSA/Ab<sub>1</sub>/GS-SnO<sub>2</sub>-PAN/GCE (curve e), B-Ab<sub>2</sub>/HIgG/BSA/Ab<sub>1</sub>/GS-SnO<sub>2</sub>-PAN/GCE (curve f), SA/B-Ab<sub>2</sub>/HIgG/BSA/Ab<sub>1</sub>/GS-SnO<sub>2</sub>-PAN/GCE (curve g), Fe<sub>3</sub>O<sub>4</sub>@APTES-B/SA/B-Ab<sub>2</sub>/HIgG/BSA/Ab<sub>1</sub>/GS-SnO<sub>2</sub>-PAN/GCE (curve h); (B) Nyquist diagrams of electrochemical impedance spectra recorded from 0.1 to 105 Hz of bare GCE (curve a), GS-SnO<sub>2</sub>-PAN/GCE (curve b), Ab<sub>1</sub>/GS-SnO<sub>2</sub>-PAN/GCE (curve c), BSA/Ab<sub>1</sub>/GS-SnO<sub>2</sub>-PAN/GCE (curve d), HIgG/BSA/Ab<sub>1</sub>/GS-SnO<sub>2</sub>-PAN/GCE (curve e), B-Ab<sub>2</sub>/HIgG/BSA/Ab<sub>1</sub>/GS-SnO<sub>2</sub>-PAN/GCE (curve f), SA/B-Ab<sub>2</sub>/HIgG/BSA/Ab<sub>1</sub>/GS-SnO<sub>2</sub>-PAN/GCE (curve g), Fe<sub>3</sub>O<sub>4</sub>@APTES-B/SA/B-Ab<sub>2</sub>/HIgG/BSA/Ab<sub>1</sub>/GS-SnO<sub>2</sub>-PAN/GCE (curve h) modified electrode in PBS containing 2.5 mM K<sub>3</sub>Fe(CN)<sub>6</sub>; (C) Comparison between multiple amplification amperometric responses of (a) one-off modified and (b) multiple replication modified electrodes.

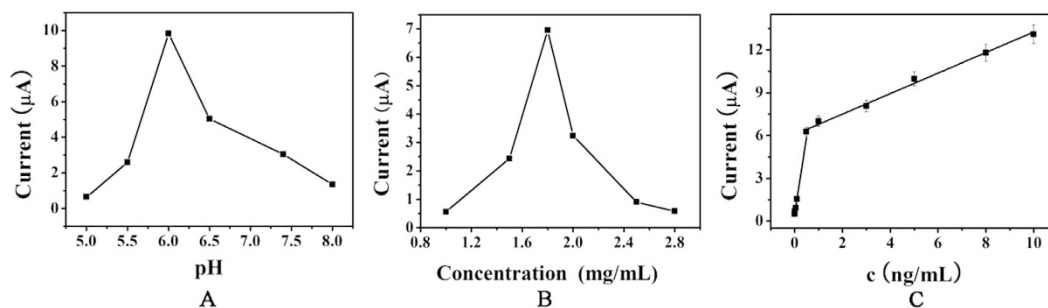


**Figure 4.** Effects of pH (A) of detection solution and concentration of Fe<sub>3</sub>O<sub>4</sub>@APTES (B) on the immunosensor. Error bar = 5%; (C) Calibration plot between the *i*-*t* current and the logarithm values of HIgG concentrations from 1 pg/mL to 0.5 ng/mL (0.001, 0.005, 0.01, 0.05, 0.1 and 0.5 ng/mL of HIgG, respectively) and from 0.5 ng/mL to 10 ng/mL (0.5, 1.0, 3.0, 5.0, 8.0, 10 ng/mL of HIgG, respectively).

To accomplish sensitive detection of HIgG, the concentration of the Fe<sub>3</sub>O<sub>4</sub>@APTES is optimized. Different concentrations of Fe<sub>3</sub>O<sub>4</sub>@APTES (0.5, 0.75, 1.0, 1.5, 1.8, and 2.0 mg/mL) are used in the fabrication of the immunosensors. Figure 4B shows that the peak current increases from 1.0 to 1.8 mg/mL of Fe<sub>3</sub>O<sub>4</sub>@APTES. Because higher concentrations of Fe<sub>3</sub>O<sub>4</sub>@APTES affect the catalytic performance in the reduction of H<sub>2</sub>O<sub>2</sub> and interface electron transfer resistance, the optimal concentration of Fe<sub>3</sub>O<sub>4</sub>@APTES is 1.8 mg/mL.

**Calibration curve.** By adopting the optimal conditions, the sandwich-type immunosensor is utilized to determine different concentrations of HIgG in the PBS solutions based on the amperometric *i*-*t* current. Figure 4C shows the amperometric *i*-*t* current of different concentrations of HIgG in the PBS with a pH of 6.0. The current response versus concentration of HIgG shows good linearity in the range between 0.001 and 0.5 ng/mL as well as 0.5 ng/mL and 10 ng/mL with a detection limit of 0.33 pg/mL (S/N = 3). The regression equations of the calibration curves are  $Y_1 = 0.4916 + 10.749 \times_1$  ( $R_1 = 0.9777$ ) and  $Y_2 = 6.0646 + 0.7194 \times_2$  ( $R_2 = 0.9901$ ), respectively. The results demonstrate quantitative detection of HIgG.

**Comparison of different methods.** Table S1 compares this method with others. The detection limit of this immunosensor is significantly lower than those of other methods. The lower detection limit is attributed to the triple amplification of SA-B-Fe<sub>3</sub>O<sub>4</sub>@APTES.

**Reproducibility, selectivity, and stability.** To investigate the precision of the measurement, the electrochemical immunosensor is used to determine 1 ng/mL of HIgG (Fig. 5A). The relative standard deviation (RSD) is 3.20% indicating good precision and reproducibility. The influence of coexisting substances on the determination of HIgG is investigated by means of the amperometric *i*-*t* currents (Fig. 5B). The interfering substances include alpha fetal protein (AFP), carcinoembryonic antigen (CEA), prostate specific antigen (PSA), and human immunoglobulin E (HIgE). Compared to HIgG (1 ng/mL), the current change caused by introduction of the four proteins is less than 5% and so the selectivity is acceptable. The stability is also investigated by keeping the electrode

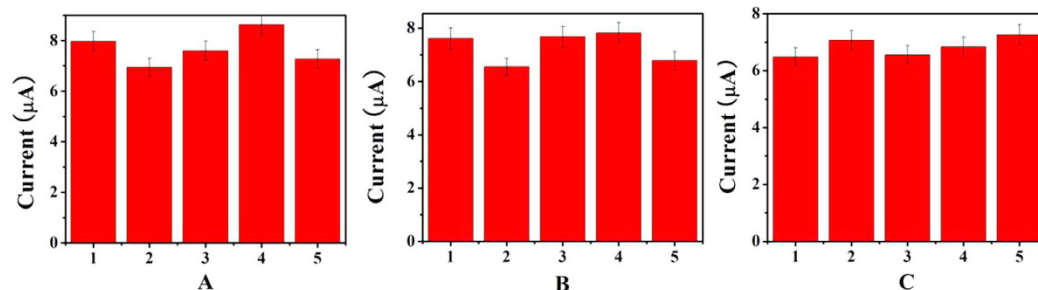


**Figure 5.** (A) Amperometric change response of the biosensor to different electrodes treated in same way to evaluate the reproducibility (RSD = 3.20%); (B) Amperometric response of the immunosensor to 1.0 ng/mL HgG (1), 1.0 ng/mL HgG + 100 ng/mL AFP (2), 1.0 ng/mL HgG + 100 ng/mL CEA (3), 1.0 ng/mL HgG + 100 ng/mL PSA (4), 1.0 ng/mL HgG + 100 ng/mL HIgE (5); (C) Stability study of the HgG immunosensor.

at 4 °C when it is not in use. Figure 5C shows that 96.3% of the initial current response is retained after 2 weeks and 89.8% after 1 month indicating good stability in the buffer solution.

**Real sample analysis.** In order to assess the clinical potential of the immunosensor, it is employed to detect the concentrations of HgG in real serum sample according to the standard addition method. Table S2 shows the experimental results showing RSD between 1.4% and 2.4% and recovery in the range from 98.8% to 100.2%. The results demonstrate that the novel sandwich-type electrochemical immunosensor based on GS-SnO<sub>2</sub>-PAN as a platform and B-Fe<sub>3</sub>O<sub>4</sub>@APTES as the label for triple signal amplification for quantitative detection of HgG has good reproducibility, selectivity, and stability and is clinically acceptable.

## Methods

**Reagents and Apparatus.** The HgG antibody (anti-HgG, 12 mg/mL) and HgG were bought from Dingguo Changsheng Biotechnology Company (Bei Jing, China) and bovine serum albumin (BSA, 96–99%) was obtained from Sigma (St. Louis, MO, USA). Streptavidin (SA) was purchased from Aladdin industrial corporation (China) and biotinamido hexanoic acid N-hydroxysuccinimide (B-NHS) ester and 3-aminopropyltriethoxysilane (APTES, 99%) were obtained from Sigma (St. Louis, MO, USA). Tin dioxide loaded graphene (SnO<sub>2</sub>-GS) (SnO<sub>2</sub> content: 50 wt%, graphene sheet size: 500 nm~5 μm) was purchased from Xian Feng Nanomaterials Technology Company (Nanjing, China) and ferric oxide (Fe<sub>3</sub>O<sub>4</sub>) was purchased from Bo Di Chemical Industry Company (Tian Jin, China). The phosphate buffered solution (PBS, pH = 7.4) was prepared using 1/15 M KH<sub>2</sub>PO<sub>4</sub> and 1/15 M Na<sub>2</sub>HPO<sub>4</sub>. The HgG was stored at 4 °C and the standard solution was prepared daily with PBS. 5 mM K<sub>3</sub>[Fe(CN)<sub>6</sub>] was used as electrolyte for all electrochemistry measurements. All other chemicals were analytical reagents grade and used without further purification.

The electrochemical measurements were carried out on a CHI 760D electrochemical workstation (Shanghai CH Instruments Co., China) and cyclic voltammetry (CV) experiments were recorded in 5 mM K<sub>3</sub>[Fe(CN)<sub>6</sub>] by scanning the potential from −0.6 V to 0.2 V. In the impedance measurements, a frequency range of 100 kHz to 0.01 Hz and AC applied potential difference amplitude of 5 mV were used. Scanning electron microscopy (SEM) was conducted on the Quanta FEG250 field emission environmental SEM (FEI, United States) at 4 kV. The FTIR spectra were acquired on the FT-IR-410 infrared spectrometer (JASCO, Japan). X-ray diffraction (XRD) was performed on the D/Max 2500V/PC diffractometer (Rigaku Corporation, Japan) with Cu K<sub>α</sub> irradiation (λ = 0.154 nm) at a scanning rate of 0.0202 θ/s and 2θ between 5° and 80°.

**Preparation of GS-SnO<sub>2</sub>-PAN composites.** The black precipitate, GS-SnO<sub>2</sub>, was dispersed in dimethyl formamide (DMF, 10 mL) and aniline (0.05 mL) and hydrochloric acid (1 mL) were added to the suspension and stirred for 1 h. Ammonium persulfate (0.114 g) was added and the solution was ultra-sonicated for 12 h. After the reaction, GS-SnO<sub>2</sub>-PAN was obtained by washing with deionized water and ethanol and drying at 60 °C in a vacuum for 24 h.

**Preparation of biotinylated antibody (B-Ab<sub>2</sub>).** The biotinylated antibody was prepared according to the procedures described by Zhao *et al.*<sup>48</sup> with some modifications as follows. The antibody solution (10 μg/mL) was produced with 1/15 mol/L PBS (pH = 7.4) and then mixed with 50 μL of 1.0 mg/mL B-NHS in dimethylsulfoxide (DMSO). The mixture was stirred for 4 h at room temperature and kept overnight at 4 °C. After dialyzing against PBS for 3 days, it was stored at 4 °C before use.

**Preparation of biotinylated magnetic nanoparticles (B-Fe<sub>3</sub>O<sub>4</sub>@APTES).** The Fe<sub>3</sub>O<sub>4</sub> nanoparticles (0.5000 g) were dispersed in ethanol/water (volume ratio 1:1, 50 mL) ultrasonically for 30 min and then APTES (6 mL, 99%) was added to the mixture under mechanical stirring at 40 °C for 8 h. The suspended magnetic nanoparticles were separated magnetically and the product (Fe<sub>3</sub>O<sub>4</sub>@APTES) was rinsed with ethanol 3 times to remove unreacted APTES molecules followed by drying at room temperature in vacuum. The Fe<sub>3</sub>O<sub>4</sub>@APTES (10.00 g) was dispersed in PBS (30 mL, pH = 7.4) and B-NHS (1 mg) dissolved in DMF (1 mL) was added under agitation. The B-Fe<sub>3</sub>O<sub>4</sub>@APTES solution was obtained after stirring at 37 °C for 12 h.

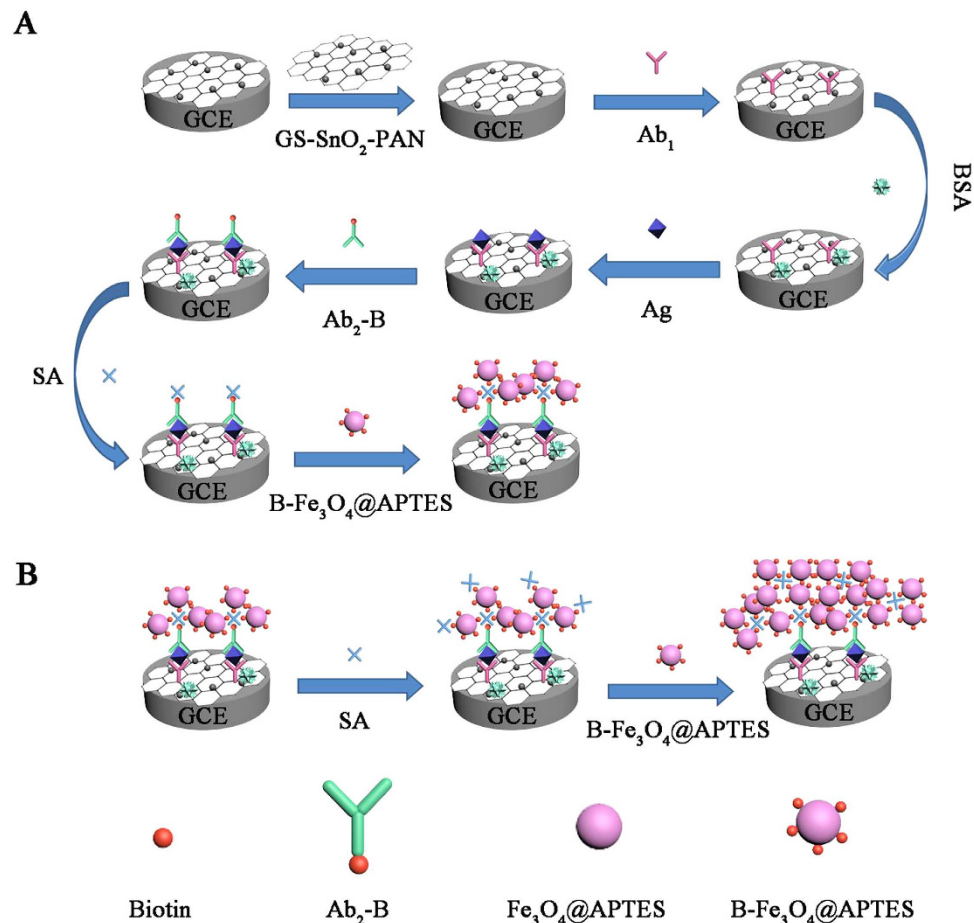


**Figure 6.** (A) Preparation procedures for the sandwich-type immunosensor and (B) Multiple amplification strategy by repeating the B–SA–B process.

**Fabrication of the immunosensor.** Figure 6A shows the process of the fabrication of the sandwich-type electrochemical immunosensor and Fig. 6B illustrates the process for multiple-amplification by repeating the B–SA–B process. Generally, the GCE was polished by alumina powders with particle size of 1.0, 0.3, and 0.05  $\mu\text{m}$  sequentially, followed by ultrasonic treatment in ethanol and rinsing with ultrapure water. The GS-SnO<sub>2</sub>-PAN (1 mg/mL, 6  $\mu\text{L}$ ) composite was put onto the pretreated electrode surface and dried. The GS-SnO<sub>2</sub>-PAN/GCE was incubated with Ab<sub>1</sub> (10  $\mu\text{g}/\text{mL}$ , 6  $\mu\text{L}$ ) and dried at 4  $^{\circ}\text{C}$ . After washing, 3  $\mu\text{L}$  of 1 wt% BSA was modified onto the electrode and incubated for 0.5 h to eliminate nonspecific binding sites. The electrode was washed and incubated with different concentrations of HlgG for 1 h at room temperature and the electrode was washed extensively to remove unbounded HlgG molecules. Subsequently, the prepared B-Ab<sub>2</sub> solution (10  $\mu\text{g}/\text{mL}$ , 6  $\mu\text{L}$ ) was added to the surface of the electrode and SA (0.1 ng/mL, 6  $\mu\text{L}$ ) was modified on the surface of the electrode. Finally, the conjugated biotin (B-Fe<sub>3</sub>O<sub>4</sub>@APTES, 2 mg/mL, 6  $\mu\text{L}$ ) was added to the surface of the electrode to produce the electrochemical immunosensor.

**Detection of HlgG.** A conventional three-electrode system was adopted in the electrochemical measurements. The GCE 4 mm in diameter was the working electrode, the saturated calomel electrode (SCE) was the reference electrode, and the platinum wire electrode served as the counter electrode. The PBS with a pH of 6.0 was used in the electrochemical measurements. CV was performed using a conventional electrochemical cell while scanning the potential from  $-0.2$  to  $0.6$  V. The amperometric  $i-t$  curve was used to monitor the electrochemical signal in PBS by scanning the potential at  $-0.4$  V and H<sub>2</sub>O<sub>2</sub> (5 M, 10  $\mu\text{L}$ ) was added to PBS (10 mL) after the current stabilized under stirring.

## References

1. Arnold, J. N., Wormald, M. R., Sim, R. B., Rudd, P. M. & Dwek, R. A. The impact of glycosylation on the biological function and structure of human immunoglobulins. *Annu. Rev. Immunol.* **25**, 21–50 (2007).
2. Campanella, L., Martini, E. & Tomassetti, M. Determination of HlgG and anti-HlgG using a single potentiometric immunosensor and two different “competitive methods”: Application to the analysis of globulin G in human serum. *Sensor. Actuator. B* **130**, 520–530 (2008).
3. Hou, S. *et al.* Exploration of attenuated total reflectance mid-infrared spectroscopy and multivariate calibration to measure immunoglobulin G in human sera. *Talanta* **142**, 110–119 (2015).
4. Qiu, L.-P. *et al.* A label-free electrochemical immunoassay for IgG detection based on the electron transfer. *Talanta* **83**, 42–47 (2010).

5. Qi, H., Wang, C. & Cheng, N. Label-free electrochemical impedance spectroscopy biosensor for the determination of human immunoglobulin G. *Microchim. Acta* **170**, 33–38 (2010).
6. Engvall, E. & Perlmann, P. Enzyme-linked immunosorbent assay (ELISA) quantitative assay of immunoglobulin G. *Immunochemistry* **8**, 871–874 (1971).
7. Soini, E. & Hemmilä, I. Fluoroimmunoassay: present status and key problems. *Clin. Chem.* **25**, 353–361 (1979).
8. Tanaka, T. & Matsunaga, T. Fully automated chemiluminescence immunoassay of insulin using antibody-protein A-bacterial magnetic particle complexes. *Anal. Chem.* **72**, 3518–3522 (2000).
9. Mayer, K. M. *et al.* A label-free immunoassay based upon localized surface plasmon resonance of gold nanorods. *ACS nano* **2**, 687–692 (2008).
10. Tang, H., Chen, J., Nie, L., Kuang, Y. & Yao, S. A label-free electrochemical immunoassay for carcinoembryonic antigen (CEA) based on gold nanoparticles (AuNPs) and nonconductive polymer film. *Biosens. Bioelectron.* **22**, 1061–1067 (2007).
11. Li, N. *et al.* A label-free electrochemical immunosensor based on Au@Pd/Ag yolk-bimetallic shell nanoparticles and amination graphene for detection of nuclear matrix protein 22. *Sensor. Actuat. B* **202**, 67–73 (2014).
12. Weng, S. *et al.* Label-free electrochemical immunosensor based on  $K_3[Fe(CN)_6]$  as signal for facile and sensitive determination of tumor necrosis factor- $\alpha$ . *Sensor. Actuat. B* **184**, 1–7 (2013).
13. Yang, Z. *et al.* A streptavidin functionalized graphene oxide/Au nanoparticles composite for the construction of sensitive chemiluminescent immunosensor. *Anal. Chim. Acta* **839**, 67–73 (2014).
14. Morales-Narváez, E. & Merkoçi, A. Graphene oxide as an optical biosensing platform. *Adv. Mater.* **24**, 3298–3308 (2012).
15. Jin, Y. & Jia, M. Design and synthesis of nanostructured graphene-SnO<sub>2</sub>-polyaniline ternary composite and their excellent supercapacitor performance. *Colloid. Surface. A* **464**, 17–25 (2015).
16. Yang, S., Feng, X., Ivanovici, S. & Müllen, K. Fabrication of graphene-encapsulated oxide nanoparticles: towards high-performance anode materials for lithium storage. *Angew. Chem. Int. Edit.* **49**, 8408–8411 (2010).
17. Lu, T. *et al.* Electrochemical behaviors of graphene-ZnO and graphene-SnO<sub>2</sub> composite films for supercapacitors. *Electrochim. Acta* **55**, 4170–4173 (2010).
18. Childs, G. & Unabia, G. Application of the avidin-biotin-peroxidase complex (ABC) method to the light microscopic localization of pituitary hormones. *J. Histochem. Cytochem.* **30**, 713–716 (1982).
19. Yang, Z., Shen, J., Li, J., Zhu, J. & Hu, X. An ultrasensitive streptavidin-functionalized carbon nanotubes platform for chemiluminescent immunoassay. *Anal. chim. acta* **774**, 85–91 (2013).
20. Lin, Z. *et al.* Development of a sensitive, rapid, biotin-streptavidin based chemiluminescent enzyme immunoassay for human thyroid stimulating hormone. *Talanta* **75**, 965–972 (2008).
21. Green, N. M. Avidin and streptavidin. *Method. enzymol.* **184**, 51 (1990).
22. Schmidinger, H., Hermetter, A. & Birner-Gruenberger, R. Activity-based proteomics: enzymatic activity profiling in complex proteomes. *Amino acids* **30**, 333–350 (2006).
23. Fugate, C. J. & Jarrett, J. T. Biotin synthase: Insights into radical-mediated carbon-sulfur bond formation. *BBA - Proteins Proteom.* **1824**, 1213–1222 (2012).
24. Zhu, C., Fang, Y., Wen, D. & Dong, S. One-pot synthesis of functional two-dimensional graphene/SnO<sub>2</sub> composite nanosheets as a building block for self-assembly and an enhancing nanomaterial for biosensing. *J. Mater. Chem.* **21**, 16911–16917 (2011).
25. Liang, J. *et al.* One-step *in situ* synthesis of SnO<sub>2</sub>/graphene nanocomposites and its application as an anode material for Li-ion batteries. *ACS appl. mater. inter.* **4**, 454–459 (2012).
26. Fan, X.-Y. *et al.* Sucrose assisted hydrothermal synthesis of SnO<sub>2</sub>/graphene nanocomposites with improved lithium storage properties. *J. Solid State Electr.* **17**, 201–208 (2013).
27. Wang, W., Hao, Q., Lei, W., Xia, X. & Wang, X. Graphene/SnO<sub>2</sub>/polypyrrole ternary nanocomposites as supercapacitor electrode materials. *RSC Adv.* **2**, 10268–10274 (2012).
28. Tang, L. *et al.* Preparation, structure, and electrochemical properties of reduced graphene sheet films. *Adv. Funct. Mater.* **19**, 2782 (2009).
29. Yan, J., Xiao, Y., Ning, G., Wei, T. & Fan, Z. Facile and rapid synthesis of highly crumpled graphene sheets as high-performance electrodes for supercapacitors. *RSC Adv.* **3**, 2566–2571 (2013).
30. Singh, V. V. *et al.* Greener electrochemical synthesis of high quality graphene nanosheets directly from pencil and its SPR sensing application. *Adv. Funct. Mater.* **22**, 2352–2362 (2012).
31. Acevedo, D. F., Rivarola, C. R., Miras, M. C. & Barbero, C. A. Effect of chemical functionalization on the electrochemical properties of conducting polymers. Modification of polyaniline by diazonium ion coupling and subsequent reductive degradation. *Electrochim. Acta* **56**, 3468–3473 (2011).
32. Mishra, A. K. & Ramaprabhu, S. Functionalized graphene-based nanocomposites for supercapacitor application. *J. Phys. Chem. C* **115**, 14006–14013 (2011).
33. Demir, A., Baykal, A., Sözeri, H. & Topkaya, R. Low temperature magnetic investigation of Fe<sub>3</sub>O<sub>4</sub> nanoparticles filled into multiwalled carbon nanotubes. *Synthetic Met.* **187**, 75–80 (2014).
34. Junejo, Y., Karaoğlu, E. & Baykal, A. Cefditorene-mediated synthesis of silver nanoparticles and its catalytic activity. *J. Inorg. Organomet. P.* **23**, 970–975 (2013).
35. Yamaura, M. *et al.* Preparation and characterization of (3-aminopropyl) triethoxysilane-coated magnetite nanoparticles. *J. Magn. Mater.* **279**, 210–217 (2004).
36. Waldron, R. Infrared spectra of ferrites. *Phys. Rev.* **99**, 1727 (1955).
37. Ma, M. *et al.* Preparation and characterization of magnetite nanoparticles coated by amino silane. *Colloid. Surface. A* **212**, 219–226 (2003).
38. Guang-She, L., Li-Ping, L., Smith, R. & Inomata, H. Characterization of the dispersion process for NiFe<sub>2</sub>O<sub>4</sub> nanocrystals in a silica matrix with infrared spectroscopy and electron paramagnetic resonance. *J. Mol. Struct.* **560**, 87–93 (2001).
39. Bruni, S. *et al.* IR and NMR study of nanoparticle-support interactions in a Fe<sub>2</sub>O<sub>3</sub>-SiO<sub>2</sub> nanocomposite prepared by a Sol-gel method. *Nanostruct. mater.* **11**, 573–586 (1999).
40. White, L. & Tripp, C. Reaction of (3-aminopropyl) dimethylethoxysilane with amine catalysts on silica surfaces. *J. Colloid Interf. Sci.* **232**, 400–407 (2000).
41. Heiney, P. A., Grüneberg, K., Fang, J., Dulcey, C. & Shashidhar, R. Structure and growth of chromophore-functionalized (3-aminopropyl) triethoxysilane self-assembled on silicon. *Langmuir* **16**, 2651–2657 (2000).
42. Lien, Y.-H. & Wu, T.-M. Preparation and characterization of thermosensitive polymers grafted onto silica-coated iron oxide nanoparticles. *J. Colloid Interf. Sci.* **326**, 517–521 (2008).
43. Tang, D., Yuan, R. & Chai, Y. Magnetic core-shell Fe<sub>3</sub>O<sub>4</sub>@Ag nanoparticles coated carbon paste interface for studies of carcinoembryonic antigen in clinical immunoassay. *J. Phys. Chem. B* **110**, 11640–11646 (2006).
44. Karaoglu, E., Summak, M., Baykal, A., Sözeri, H. & Toprak, M. S. Synthesis and Characterization of Catalytically Activity Fe<sub>3</sub>O<sub>4</sub>-3-Aminopropyl-triethoxysilane/Pd Nanocomposite. *J. Inorg. Organomet. P.* **23**, 409–417 (2013).
45. Wu, W., He, Q. & Jiang, C. Magnetic iron oxide nanoparticles: synthesis and surface functionalization strategies. *ChemInform* **40**, i (2009).
46. Katz, E. & Willner, I. Switching of directions of bioelectrocatalytic currents and photocurrents at electrode surfaces by using hydrophobic magnetic nanoparticles. *Angew. Chem.* **117**, 4869–4872 (2005).

47. Gao, J. *et al.* Ultrasensitive enzyme-free immunoassay for squamous cell carcinoma antigen using carbon supported Pd–Au as electrocatalytic labels. *Anal. Chim. Acta* **833**, 9–14 (2014).
48. Wang, L., Zhang, Y., Gao, X., Duan, Z. & Wang, S. Determination of chloramphenicol residues in milk by enzyme-linked immunosorbent assay: improvement by biotin-streptavidin-amplified system. *J. Agr. Food Chem.* **58**, 3265–3270 (2010).

### Acknowledgements

This study was supported by the National Natural Science Foundation of China (No. 21575079; 21405095; 21575050), Project of Shandong Province Higher Educational Science and Technology Program (No. J14LC09), and City University of Hong Kong Applied Research Grant (ARG) No. 9667104.

### Author Contributions

Y.L., Y.Z. and Q.W. conceived and designed the experiments. L.J. and Y.L. performed the experiments, analyzed the data and wrote the first draft of the manuscript. P.C., Y.D. and Q.W. contributed substantially to revisions.

### Additional Information

**Supplementary information** accompanies this paper at <http://www.nature.com/srep>

**Competing financial interests:** The authors declare no competing financial interests.

**How to cite this article:** Li, Y. *et al.* A sandwich-type electrochemical immunosensor based on the biotin-streptavidin-biotin structure for detection of human immunoglobulin G. *Sci. Rep.* **6**, 22694; doi: 10.1038/srep22694 (2016).



This work is licensed under a Creative Commons Attribution 4.0 International License. The images or other third party material in this article are included in the article's Creative Commons license, unless indicated otherwise in the credit line; if the material is not included under the Creative Commons license, users will need to obtain permission from the license holder to reproduce the material. To view a copy of this license, visit <http://creativecommons.org/licenses/by/4.0/>